PHYSICAL REVIEW B **79**, 134438 (2009)

Complementary polarized neutron and resonant x-ray magnetic reflectometry measurements in Fe/Gd heterostructures: Case of inhomogeneous intralayer magnetic structure

E. Kravtsov,[1] D. Haskel,[1] S. G. E. te Velthuis,[2] J. S. Jiang,[2] and B. J. Kirby[3]
[1]*Advanced Photon Source, Argonne National Laboratory, Argonne, Illinois 60439, USA*
[2]*Materials Science Division, Argonne National Laboratory, Argonne, Illinois 60439, USA*
[3]*NIST Center for Neutron Research, Gaithersburg, Maryland 20899, USA*

(Received 17 December 2008; revised manuscript received 18 March 2009; published 30 April 2009)

A unified approach combining polarized neutron and resonant x-ray magnetic reflectometry has been applied to determine the magnetic structure in an $[\mathrm{Fe}(35\text{ Å})/\mathrm{Gd}(50\text{ Å})]_5$ multilayer as a function of temperature and magnetic field. Simultaneous self-consistent refinement of neutron and x-ray data made it possible to resolve the element-specific magnetization profile in the multilayer with unprecedented accuracy. It is shown that the small number of bilayer periods together with the asymmetric termination (Fe-top, Gd-bottom) lead to unique low-temperature magnetic phases characterized by significant twisting of Fe and Gd magnetic moments and nonuniform distribution of vectorial magnetization within Gd layers. A twisted magnetic state was found to be stable at small magnetic fields and at a low temperature of 20 K, which is well below the compensation temperature of this artificial ferrimagnetic system.

DOI: 10.1103/PhysRevB.79.134438 PACS number(s): 75.75.+a, 61.05.fj, 61.05.cm

I. INTRODUCTION

There has been great interest in artificial magnetic nanostructures displaying a rich variety of novel phenomena and acquiring importance for technological applications. Fe/Gd multilayers are ideal model systems showing complex magnetic behavior.[1] Unlike similar systems Co/Gd (Ref. 2) and Ni/Gd,[3] Fe/Gd interfaces are quite sharp due to negligible Fe-Gd interdiffusion,[4] which makes it possible to grow superlattices with nearly perfect layered structure. Various magnetic configurations in Fe/Gd arise from the competition between Zeeman interaction, strong antiferromagnetic Fe-Gd interfacial coupling, and intralayer exchange coupling, which is relatively weak inside Gd and strong inside Fe. The strong temperature dependence for the Gd magnetic moment ($T_C = 293$ K) and relatively weak one for Fe ($T_C = 1043$ K) result in a complex magnetic phase diagram with varying temperature and applied magnetic field.[5–7] Furthermore, an Fe-Gd proximity effect results in enhancement of the Gd ordered magnetic moment near Gd/Fe interfaces.[8] Intralayer crystallographic structure in Fe/Gd superlattices remains disordered or "amorphous" until Fe thickness exceeds some critical value about 21–23 Å, above which a sharp transition to a polycrystalline bcc state occurs in the Fe layers, with Gd remaining disordered at all layer thicknesses.[4,9] This ordering transition is accompanied by a corresponding sharp increase in grain size. Magnetocrystalline anisotropy, which generally plays an important role in magnetic multilayers, is almost negligible in Fe/Gd due to the polycrystalline or disordered character of the Fe/Gd layers.

To date, a majority of attention has focused on Fe/Gd multilayers with a large number of repetitions. Theoretical calculations performed by Camley *et al.*[5–7] for Fe/Gd superlattices with an infinite number of repetitions have predicted the existence of three phases: Gd-aligned, Fe-aligned, and twisted. The Gd-aligned phase, with Gd (Fe) magnetic moments aligned along (opposite) the applied magnetic field is stable at low temperatures where the Gd net magnetic moment dominates. At high temperatures, where the Fe magnetic moment dominates, there exists the Fe-aligned phase with the Fe (Gd) moments oriented along (opposite) the field. The twisted phase, featuring in-plane canting of Fe and Gd magnetic moments, appears at temperatures close to the compensation temperature, where the Gd and Fe net magnetic moments are close to each other. A twisted phase can also be produced from an aligned phase by applying a strong enough magnetic field.

The above theoretical picture has been confirmed by numerous experiments on Fe/Gd superlattices. Depth-resolved techniques, such as polarized neutron reflectometry (PNR) (Refs. 10–13) and resonant x-ray magnetic reflectometry (RXMR),[8,14–16] have been successfully applied to resolve magnetization profiles in Fe/Gd and provide experimental evidence for the theoretical models discussed above. Thermal magnetic hysteresis transition between Gd- and Fe-aligned states was observed in Fe/Gd superlattices and described in terms of these models.[17,18] It was also found[8,16] that the magnetization density profile inside Gd layers becomes nonuniform at high temperatures, with the Gd magnetic moment enhanced at the Fe/Gd interfaces and reduced in the core of the Gd layers. Similar behavior was also reported for other Gd-based systems, for example, Co/Gd,[17] CoGd/Gd,[19] and Ni/Gd.[20]

Whereas the magnetic phase diagram is well established for Fe/Gd multilayers with a large number of repetitions, the systems with a small number of repetitions have been seldom studied. Broken symmetry at interfaces, finite-size effects, and asymmetric termination of the layers stack (different layers at the top and bottom) should play increasingly important roles in these structures, resulting in novel magnetic configurations. Recent micromagnetic simulations[21] have provided some examples of hypothetical Fe/Gd model systems where finite-size effects result in the development of a complex domain structure inside Gd, i.e., an inhomogeneous intralayer Gd magnetic structure, which, in turn, leads to novel ground states. These include twisted ground states with magnetic moments rotated away from the direction of the applied magnetic field, even at very small fields.

In order to understand and utilize the physical mechanisms responsible for novel properties of magnetic heterostructures, it is important to precisely resolve (at subnanometer scale) inhomogeneous magnetization density depth profiles, which are typical in these structures. The most powerful techniques to probe magnetization depth profiles in multilayered nanostructures are polarized neutron reflectometry and resonant x-ray magnetic reflectometry. Both techniques are well established and have been successfully applied to resolve in-depth magnetization distributions in magnetic heterostructures.[10,22]

The main advantage of the PNR technique is its ability to directly probe atomic magnetic moments and provide information about the in-plane magnetic moment in absolute units. On the other hand, this technique is not element specific and, due to low incoming neutron beam flux, has limited spatial resolution. In the case of magnetic heterostructures, PNR can detect local variations in the magnetic moment, and PNR spectra can be described by using model magnetization profiles convoluted with the nominal experimental resolution function. Although the spatial resolution is limited, PNR is often able to resolve variations in magnetic moments over spatial regions smaller than the nominal experimental resolution as estimated from the highest measured Q value,[23] but the lack of a systematic way to refine magnetization profiles beyond the nominal experimental resolution remains a problem. However, if possible solutions can be generated independently, PNR becomes an efficient tool in selecting the proper solution. In the particular case of Fe/Gd heterostructures, there is an additional complication with using neutrons as the probe. Generally, neutron-scattering cross sections are well known for thermal neutrons and do not depend on the neutron energy. Gd is a remarkable exception; its neutron-scattering cross sections are highly energy dependent due to strong resonant absorption observed in the thermal energy region, with the neutron-scattering lengths of every Gd isotope having different energy dependence.[24] In fact, small variations in the Gd isotopic composition would affect strongly the Gd neutron-scattering cross sections. Practically, it is important to perform additional calibrations in order to determine Gd neutron-scattering lengths for a particular system.

When applied in the hard x-ray regime, RXMR utilizes resonant enhancement for the x-ray magnetic scattering observed at K edges of transition metals and L edges of rare earths. RXMR provides both element sensitivity and high spatial resolution due to the high flux of synchrotron radiation. However, when working with circularly polarized x rays, it detects only the in-plane component of magnetic moment within the scattering plane. Sometimes it may be possible to measure with RXMR the second in-plane component by rotating the sample and magnetic field by 90°. Due to the indirect nature of the photon interaction with magnetic moments, x-ray resonant magnetic scattering cross sections in the hard x rays tend to be rather weak and depend on the particular local structure, which makes it necessary to perform additional absorption measurements in order to determine the proper scattering lengths. In addition, it is not always possible to probe all the elements in heterostructures and gain complete information on the system.

The weakness of both PNR and RXMR techniques lies in the absence of the phase information in the measured scattered intensity. It is then not possible to find the unique solution for the magnetization profile. RXMR with circularly polarized x rays, being related to charge-magnetic interference scattering,[25] depends on variations of both chemical and magnetic density profiles, with charge scattering cross sections being several orders of magnitude stronger than the magnetic ones. Hence, uncertainty in chemical structure determination will affect the magnetic structure solution. In the case of complex magnetic systems, where both long- and short-range variations in magnetic moments are present, RXMR is often more sensitive to short-range variations since small penetration depth at angles near the total reflection region (small Q's) limits its sensitivity to long-range modulations in magnetization profiles, including the integrated magnetic moment. In contrast to RXMR, PNR is highly sensitive to long-range variations in magnetic moments, especially to the integrated magnetic moment. The complementary use of PNR and RXMR to determine complex magnetization profiles in Fe/Gd allows us to mitigate the weaknesses of both methods and emphasize their strengths. Simultaneous refinement of PNR and RXMR spectra helps us to select reliable models to describe the element-specific magnetization profiles in Fe/Gd.

In the present paper, we provide direct experimental evidence of the nature of twisted ground states that occur in $[\mathrm{Fe}(35\ \text{Å})/\mathrm{Gd}(50\ \text{Å})]_5$ heterostructures at rather low temperatures (20 K), i.e., well below the compensation temperature of the system (60 K). Similar multilayers consisting of 15 Fe/Gd bilayers have been studied in detail,[8,12,14–16] and their magnetic phase diagram was shown to comply with the theoretical predictions of Camley *et al.*[5–7] Our approach entails performing complementary polarized neutron reflectometry and resonant x-ray magnetic reflectometry measurements, followed by simultaneous refinement of the experimental neutron and x-ray spectra within a unified parametrized model. This procedure allows us to gain high-precision, depth-resolved, element-specific magnetization profiles in magnetically inhomogeneous Fe/Gd heterostructures. The detailed depth-resolved magnetic information provided by this complementary approach cannot be obtained by applying these techniques separately. The integrated net magnetic moment in the system is shown to be consistent with independent magnetometry and x-ray magnetic circular dichroism (XMCD) data.

II. EXPERIMENTAL

The $[\mathrm{Fe}(35\ \text{Å})/\mathrm{Gd}(50\ \text{Å})]_5$ multilayer was grown via magnetron UHV sputtering onto a Si substrate with Al buffer (100 Å) and cap (50 Å) layers. Fe and Gd growth rates were kept at 1–2 Å/s with the base chamber pressure 1.8×10^{-8} Torr. The sample was cut into two pieces to be used independently in magnetometry measurements and neutron and x-ray studies. The structural properties of the multilayer were characterized with x-ray reflectometry car-

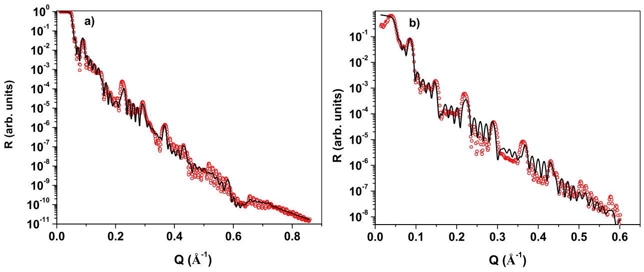

FIG. 1. (Color online) Experimental (circles) and corresponding theoretical (line) x-ray reflectivity curves taken from the [Fe(35 Å)/Gd(50 Å)]$_5$ multilayer (a) at off-resonance conditions ($E=6500$ eV) and (b) at energy $E=7929$ eV (Gd L_2 resonance). Well-defined Bragg peaks up to the fifth order suggest highly correlated layer structure throughout the multilayer.

ried out at beamline 4ID-D of the Advanced Photon Source at Argonne National Laboratory. These x-ray measurements were performed at nonresonant conditions ($E=6500$ eV), far from Gd and Fe resonances as well as at the Gd L_2 absorption edge ($E=7929$ eV). The nonresonant scans were carried out at room temperature with linear σ-polarized light, and resonant scans were also performed at temperatures $T=140$ K and $T=20$ K with circularly polarized light and averaged over the two opposite helicities.

The resonant and nonresonant reflectivity scans were simultaneously fitted with the same structural model (Fig. 1). The Gd scattering lengths at $E=7929$ eV were determined experimentally with complementary absorption measurements as discussed below. Tabulated scattering lengths were used for the nonresonant elements.[26] The results of the structural refinement are presented in Table I. In the refinement, all Fe and Gd layers in the multilayer stack were assumed to be identical except for the very bottom Gd layer grown directly on the Al buffer, which was found partly alloyed with the buffer layer. A similar Al-Gd alloying effect was also reported in other Al/Gd layered systems.[27] We note good layer structure in the system and low interfacial roughness between Fe and Gd. The thickness of the buffer Al layer has large uncertainty due to the small difference between the Al and Si scattering lengths. Because of the small incidence angles, the x-ray footprint on the sample is much larger than the grain size so effects from granular structure are described via contributions to surface and interface roughness.

TABLE I. Structural properties of [Fe(35 Å)/Gd(50 Å)]$_5$ multilayer according to the refinement of x-ray scans.

Layer	Thickness [Å]	rms roughness [Å]
Al_2O_3	45.1(2)	4.5(2)
Al	5.4(6)	1.9(4)
Fe (multilayer stack)	38.4(6)	1.3(6)
Gd (multilayer stack)	48.4(3)	4.7(8)
Gd (last layer in the stack)	22.9(7)	4.3(9)
Gd_2Al_3	27.5(7)	1.6(6)
Al (buffer)	91(10)	4.4(9)

Magnetometry measurements were performed with a superconducting quantum interference device (SQUID). The RXMR and XMCD measurements were performed at undulator beamline 4ID-D of the Advanced Photon Source at Argonne National Laboratory. Magnetic reflectivity scans were done at the Gd-L_2 absorption edge with photon energy $E=7929$ eV. A double-crystal Si(111) monochromator was used to select the particular wavelength of linearly polarized synchrotron radiation, which was then converted to circular polarization with a diamond (111) quarter-wave plate operated in Bragg transmission geometry.[28,29] The sample was mounted on a variable temperature insert cooled with liquid He, and placed in the bore of a 4 T superconducting magnet mounted on a four-circle diffractometer. The magnetic reflectivity was measured as the difference between reflected intensities for two opposite helicities (R_+-R_-). The XMCD measurements were performed in fluorescence mode by detecting the difference in absorption for two opposite helicities while scanning the photon energy through the Gd L_2 absorption edge. The PNR measurements were performed at the NG1 reflectometer at the NIST Center for Neutron Research. The NG1 measurements were done in standard θ-2θ geometry with constant neutron wavelength of 4.75 Å, with full polarization analysis being performed. The sample was mounted in a closed cycle refrigerator placed in an electromagnet. The scattered neutrons were detected with a linear pencil detector, allowing detection of specularly scattered neutrons only. The neutron and RXMR measurements were performed at $T=20$ K for two values of the magnetic field: $H=50$ and 500 mT. An additional calibration measurement was done at $T=140$ K in a magnetic field of $H=50$ mT. In order to prepare the magnetic state, the sample was field cooled from room temperature in $H=500$ mT; the magnetic field was then reduced to the target value. The field-cooling procedure was done in strong enough magnetic fields in order to suppress possible thermal hysteresis effects.[17,18] Temperature dependence of the net magnetic moment measured with SQUID in this magnetic field did not show any hysteresis when measured with ascending and descending temperatures. In the neutron experiments, the magnetic field was applied perpendicular to the horizontal scattering plane, with the neutron quantization axis being along the field. In x-ray experiments, the magnetic field was applied in the horizontal scattering plane. In both geometries the magnetic field is within the plane of the sample.

III. ELEMENT-SPECIFIC MAGNETOMETRY: SQUID AND XMCD

The element-specific, sample-averaged magnetic properties were determined by combining SQUID and XMCD magnetometry. Conventional magnetometry provides information on the net magnetic moment of the system in absolute units, while the integrated Gd XMCD signal is proportional to the depth-averaged Gd magnetic moment. By combining information from both measurements, one obtains the element-specific net magnetic moment of the system in absolute units. The integrated magnetic signal measured with SQUID and XMCD can change due to different effects: re-

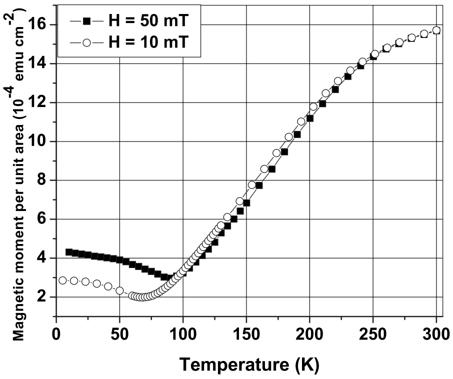

FIG. 2. Temperature dependence of the magnetic moment per unit area for $[\mathrm{Fe}(35\ \text{Å})/\mathrm{Gd}(50\ \text{Å})]_5$ multilayer measured under applied magnetic fields (Ref. 30) of 10 and 50 mT. The minimum of $M(T)$ dependence is at about 90 K for $H=50$ mT and at about 65 K for $H=50$ mT. The compensation temperature T_{comp} for zero magnetic field is then estimated to be about 60 K.

duction in the value of Gd magnetic moment, for example, due to defects, the Gd-Fe proximity effect, and twisting, i.e., rotation of magnetic moments away from the direction of magnetic field.

Figure 2 shows the temperature-dependent SQUID-magnetization data for magnetic fields of 10 and 50 mT. The change in magnetization with temperature is mainly due to variation in the ordered Gd magnetic moment, which in bulk Gd changes from $7.55\mu_B$ at 0 K to zero at 293 K. The minimum of the net magnetic moment at about 65 K in the 10 mT curve corresponds to the compensation temperature T_{comp} of the system, where the total Gd and Fe magnetic moments are nearly compensated. Hysteresis loops measured at 60 K near the compensation temperature and far from it (20 and 140 K) are depicted in Fig. 3.

The magnetic hysteresis of Fig. 3(c) shows magnetic behavior typical of the Fe-aligned phase. The essential feature is the flat region in the hysteresis loop where there is no change in the net magnetic moment with increasing magnetic field. This region represents a "true" Fe-aligned state with Fe (Gd) moments along (opposite) the applied magnetic field. As the magnetic field becomes strong enough (about 300 mT), a twisted state starts to develop with magnetic moments rotating away from the direction of magnetic field. Similar magnetic behavior was reported in Fe/Gd multilayers with the same Fe and Gd thicknesses but with a larger (15) number of repetitions.[16] The hysteresis loop measured at 20 K [Fig. 3(a)] is not what is expected for a Gd-aligned phase reported in Ref. 16 and resembles that measured near compensation [Fig. 3(b)]. This becomes more evident when we compare SQUID and XMCD data. Figure 4 shows the XMCD signal measured at different magnetic fields from 0 to 500 mT at 20 K and measured in the Fe-aligned state ($T=140$ K, $H=-50$ mT). The magnetic state during the XMCD measurement was prepared in the following way: the sample was field cooled from room temperature in $H=500$ mT, and the magnetic field was decreased to the target value when at the base temperature. The measurements were performed for opposite directions of magnetic field, the reported XMCD signal being half of the difference between XMCD signals measured for positive and negative field directions. Table II summarizes the values of the net magnetic moment and XMCD signal as extracted from the data presented in Figs. 2–4.

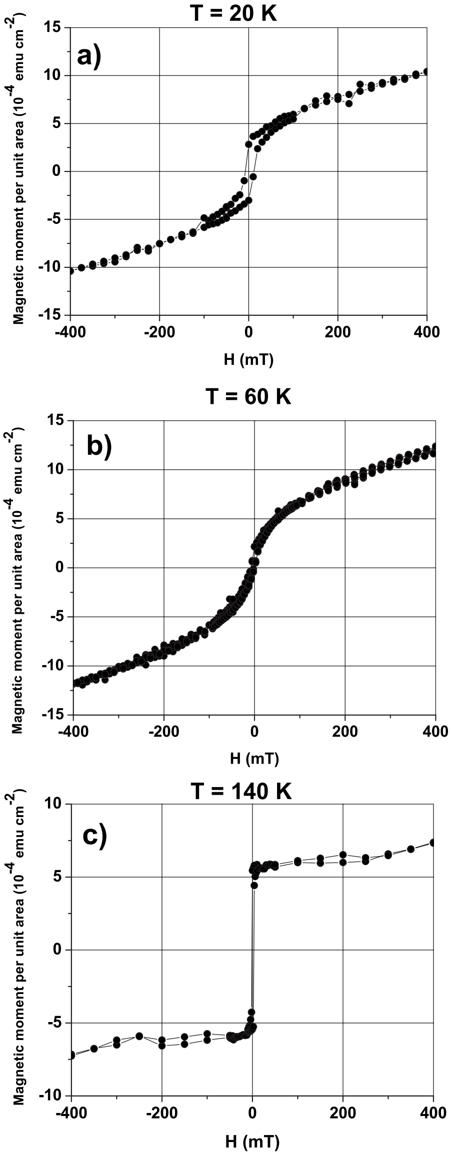

FIG. 3. Hysteresis loops for the $[\mathrm{Fe}(35\ \text{Å})/\mathrm{Gd}(50\ \text{Å})]_5$ multilayer measured in the Fe-aligned phase (140 K), at the compensation temperature (60 K), and at low temperature far from the compensation (20 K).

Based on the results of Table II, we can make preliminary estimates of the magnetic properties of the system and show that the magnetic behavior observed at 20 K is inconsistent with the presence of a Gd-aligned phase. For our estimates we take bulk saturation values for Fe and Gd magnetic moments. Bulk Gd at zero temperature has magnetic moment of $7.55\mu_B$ per atom, which corresponds to the saturation magnetization $M_s(\mathrm{Gd})=2010$ emu cm^{-3}. Iron has magnetic moment of $2.22\mu_B$ per atom, which gives the saturation magnetization $M_s(\mathrm{Fe})=1740$ emu cm^{-3}. Then the total saturated Fe and Gd magnetic moments per unit area in the multilayer will be $M_{\mathrm{Fe}}=33.4\times10^{-4}$ emu cm^{-2}; and $M_{\mathrm{Gd}}=48.6$

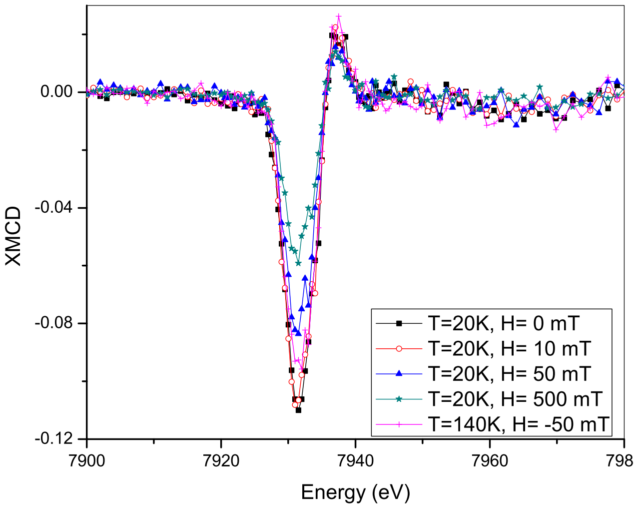

FIG. 4. (Color online) Gd L_2 edge XMCD measured at temperature $T=20$ K for different values of the applied magnetic field and at temperature 140 K and magnetic field $H=-50$ mT. The integrated XMCD signal was used as a measure of the relative net Gd moment in the multilayer.

$\times 10^{-4}$ emu cm^{-2}. If we assume that at remanence, where the Gd XMCD signal maximizes, there exists a Gd-aligned state, then in order to satisfy SQUID results, the Gd magnetic moment should be reduced ~25%. Such a reduction in Gd moment in Fe/Gd is sometimes reported in the literature[12,31] based on low-temperature magnetometry results. If we use this reduced value of M_{Gd} and the temperature dependence as obtained by XMCD, we then expect for the Gd and Fe net moments at $T=140$ K to be $M_{\mathrm{Gd}}(140\text{ K})=30.7\times 10^{-4}$ emu cm^{-2} and $M_{\mathrm{Fe}}(140\text{ K})=36.5\times 10^{-4}$ emu cm^{-2}, respectively, i.e., the Fe magnetic moment would increase to $2.43\mu_B$ per atom, which is unlikely. Hence, the comparative analysis of XMCD and SQUID results brings one to the conclusion that the Gd-aligned phase does not exist at any temperature and moderate magnetic field in our system. The low-temperature magnetization profile in this system could be inhomogeneous at all magnetic fields, including possible depth variations in both the magnitude and direction of Fe and Gd magnetic moments. The element-specific averaged magnetic moments per unit area can be obtained from the data of Table II, provided we have element-specific magnetic data for any temperature or field point from complementary measurements. Such information was provided by depth-resolved techniques (PNR and RXMR), where the Fe-aligned state (140 K) was used for calibration purposes.

TABLE II. Net magnetic moment per unit area of the sample and integrated XMCD signal from [Fe(35 Å)/Gd(50 Å)]$_5$ multilayer measured at the Gd L_2 absorption edge.

T (K)	H (mT)	M (10^{-4} emu cm^{-2})	XMCD (rel. units)
20	0	2.91	1.0
20	50	4.76	0.77
140	−50	5.86	0.89

IV. DEPTH-RESOLVED MAGNETOMETRY: PNR AND RXMR

A. Data analysis

The data analysis involves simultaneous refinement of experimental spectra for polarized neutrons and x rays. The calculation scheme is based on using a unified parametrization of chemical- and element-specific in-plane magnetization profiles in the multilayer. The RXMR signal measured with circularly polarized x rays depends on the depth variation in the chemical density throughout the multilayer as well as on the depth variation in the component of the magnetic moment in the scattering plane for the resonant element. The PNR technique is sensitive to the chemical density variation as well as the variation in both in-plane components of magnetic moments for all the multilayer constituents. In order to parametrize the depth-dependent, element-specific magnetic moments $\mathbf{M}(z)$ inside layers, we assume that it can be described with two quantities: the magnitude of the magnetic moment $M(z)$ and the angle $\theta(z)$ relative to the applied magnetic field.

In order to describe the distribution of magnetic moments inside layers, we used the following parametrization:

$$M(z) = M_0 + \frac{\sinh[|t-2z|/2\tau]}{\sinh[t/2\tau]} \times[(M_T - M_0)\,\eta(t-2z) + (M_B - M_0)\,\eta(2z-t)], \tag{1}$$

$$\theta(z) = \theta_0 + \frac{\sinh[|t-2z|/2\tau_1]}{\sinh[t/2\tau_1]} \times[(\theta_T - \theta_0)\,\eta(t-2z) + (\theta_B - \theta_0)\,\eta(2z-t)], \tag{2}$$

where $\eta(x)$ is the Heaviside step function; t is the layer thickness; M_T, M_B, and M_0 are values of the magnetic moment at the top, bottom, and in the middle of the layer, respectively; and θ_T, θ_B, and θ_0 are the directions of magnetic moments at the top, bottom, and in the middle of the layer, respectively. The parameters τ and τ_1 describe the rate of the change in the magnitude and angle of the magnetic moment inside the layer.

The PNR spectra were calculated within an approach[32] where the system was split into a set of thin sublayers with uniform atomic and magnetic neutron scattering length. To calculate RXMR spectra we used an approach similar to that developed by Stepanov *et al.*[35,36] that was modified in order to account for inhomogeneous distribution of magnetic moments inside Gd layers without splitting the system into sublayers. The description of this calculation scheme is given in the Appendix. In order to refine the model parameters, we use nonlinear least-squares fitting procedures, based on the χ^2 test.[37] The least-squares statistical sum is defined as $\chi^2 = P\cdot\chi_N^2 + (1-P)\cdot\chi_X^2$, where P is the weighting parameter. Here χ_N^2 and χ_X^2 are reduced neutron and x-ray least-squares values, respectively, as defined below. The reduced least-squares sum for neutrons χ_N^2 is constructed from the difference between experimental and theoretical data values of the PNR coefficients R,

$$\chi_N^2 = \sum_{ss'} \sum_j \frac{[R_{\text{exp}}^{ss'}(Q_j) - R_{\text{theor}}^{ss'}(Q_j)]^2}{\sigma_{ss'}(Q_j)^2}, \tag{3}$$

where $ss' = ++, --, +-$; Q_j are momentum-transfer values; and σ's are statistical uncertainties for corresponding neutron experimental data points. The reduced least-squares sum for x rays χ_X^2 is constructed from the difference between the RXMR signals for opposite helicities $\Delta R = (R_+ - R_-)$ for experimental and theoretical data values,

$$\chi_X^2 = \sum_j \frac{[\Delta R_{\text{exp}}(Q_j) - \Delta R_{\text{theor}}(Q_j)]^2}{\sigma(Q_j)^2}. \tag{4}$$

The multidimensional minimization is performed by using the minimization package MINUIT, freely available from the CERN computing department.[38] The description of calculation details and fitting procedures will be published elsewhere.

B. Determination of x-ray and neutron-scattering lengths

As discussed above, in order to perform data analysis one needs to determine the neutron and x-ray scattering lengths of Gd. The charge part of the Gd x-ray resonant scattering factor f_e depends on the local atomic structure and can be determined with absorption (x-ray absorption near edge structure) measurements. The imaginary part of the charge scattering factor f_e'' is related to the Gd absorption spectrum via the optical theorem and can be determined precisely by normalizing the measured absorption spectrum to the Gd tabulated scattering factors away from resonance.[39] The real part f_e' is then obtained by performing a differential Kramers-Krönig transform.[16,40] The tabulated and experimentally derived charge scattering factors are shown in Fig. 5(a). In particular, at the photon energy $E = 7929$ eV, the resonant charge scattering factor is $f_e = -17.53 + i \cdot 12.30$. The charge scattering factor reported for Fe/Gd multilayers of similar composition[8,16] ($f_e = -17.3 + i \cdot 13.4$) is close to this result.

For the electric-dipole transition at the L_2 absorption edge, the magnetic scattering factor f_m is related to the Gd $5d$ magnetic moment, which is strongly affected by $4f$ moments via $4f-5d$ exchange coupling. In our consideration, we assume f_m to be proportional to the Gd magnetic moment; the actual scaling factor is generally unique for a particular system. In order to derive the magnetic scattering factors, we used the XMCD spectrum measured in remanence at $T = 20$ K (Fig. 4) and follow the same procedure assuming f_m to be zero away from resonance. For the photon energy $E = 7929$ eV, we found that $f_m = 0.211 - i \cdot 0.177$. For comparison, $f_m = 0.22 - i \cdot 0.26$ was reported for Fe/Gd multilayers in Refs. 8 and 16. Since there is no evidence for the Gd magnetization being saturated at $T = 20$ K, the derived value of f_m needs to be calibrated against Gd magnetization given in absolute magnetization units.

The spin-dependent neutron-scattering length densities $\rho_\pm$ are defined as[32–34]

$$\rho_\pm = N(b_N \pm sM), \tag{5}$$

where N is the atomic density, b_N is the atomic coherent scattering length, M is the atomic magnetic moment density (in μ_B), and $s = 2.695 \times 10^{-6}$ nm/μ_B. As discussed above, in the case of Gd, the atomic coherent scattering length has a very large imaginary part and may be significantly different from the tabulated value. On the other hand, the magnetic part of the scattering length density is well defined and directly related to the Gd magnetic moment in absolute units. Since the Gd magnetization profile could be highly inhomogeneous both in magnitude and direction, at all temperatures and all magnetic fields, the Gd atomic coherent scattering length is difficult to determine from the PNR experiment alone.

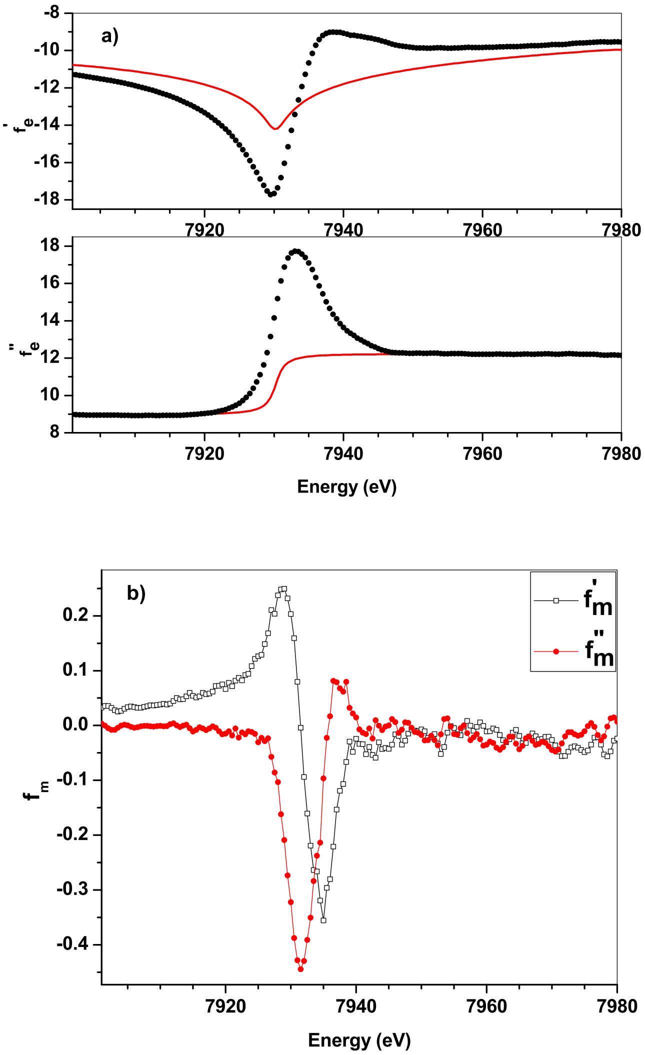

FIG. 5. (Color online) (a) Experimentally derived (circles) and tabulated (lines) (Ref. 39) charge resonant scattering factors across the Gd L_2 absorption edge. (b) Experimentally derived Gd magnetic scattering factors across the Gd L_2 absorption edge.

In order to determine precisely the neutron and x-ray scattering lengths, we performed a calibration measurement in the Fe-aligned state ($T = 140$ K, $H = 50$ mT). In this magnetic state, the Fe and Gd magnetic moments are collinear [Fig. 3(c)], and an intralayer variation in the magnitude of Gd magnetic moment due to the Gd-Fe proximity effect is present. In Fe/Gd superlattices, the magnitude of Gd magnetic moment was reported to be enhanced in a 4 Å region near Gd/Fe interfaces and reduced in the center of the layer.[8,16] In Fig. 6(a) we show the RXMR scan (asymmetry ratio) measured for positive and negative magnetic field directions. The RXMR signal is of magnetic origin and changes sign when switching the magnetic field. The PNR measurement [Fig. 6(c)] shows negligible signal in the spin-flip channel, which confirms purely collinear ordering in the system. The RXMR data set [Fig. 6(b)] was fitted in relative magnetization units by using the structural information from Table I and the x-ray scattering lengths f_e, f_m reported above. The direction of the Gd magnetic moment was fixed to be opposite to the applied magnetic field, and only the magnitude of the Gd moment [Eq. (1)] was allowed to vary. Next, the refined *relative* Gd magnetization profile was fixed and the PNR spectra were fitted by using refined x-ray structural and magnetic information. The only parameters allowed to vary were the magnitude of the Fe magnetic moment, the atomic Gd coherent scattering length, and the scaling factor for the Gd magnetic moment. The PNR spectra were satisfactorily fitted [Fig. 6(c)] with the following parameters: Fe magnetic moment $M_{\mathrm{Fe}}=2.22\mu_B$ and Gd atomic coherent scattering length density $Nb_N=(1.8779+i\cdot 3.4478)\times 10^{-5}$ Å^{-2}. The magnetic x-ray scattering factor f_m determined from the XMCD spectra measured in remanence at $T=20$ K (Fig. 4) is found to correspond to the Gd magnetic moment reduced by the factor 1.182 relative to the saturated bulk Gd magnetic moment (i.e., about $6\mu_B$ instead of $7.55\mu_B$). The Gd x-ray magnetic scattering factors renormalized to correspond with fully saturated bulk Gd values are shown in Fig. 5(b). The refined magnetization profile inside the Gd layers is depicted in Fig. 7(a). The magnetic moment of Gd was found to reach $7.23(6)\mu_B$ at Fe/Gd interfaces and $2.45(6)\mu_B$ in the middle of the Gd layers, the characteristic rate of the magnetic-moment change $\tau=3.915(4)$ [see definition in Eq. (1)]. It is important to note that the PNR spectra were found to be highly sensitive to the nonuniform magnetization profiles inside the Gd layers and cannot be correctly fitted if one tries to use constant (averaged over the Gd layer) magnetization densities. The shift in the second Bragg-peak position at $Q=0.146$ Å^{-1} for R_{++} and R_{--} seen in Fig. 6(c) is due to inhomogeneous structure inside the Gd layers and cannot be reproduced by working with a model of layer-averaged magnetic moments.

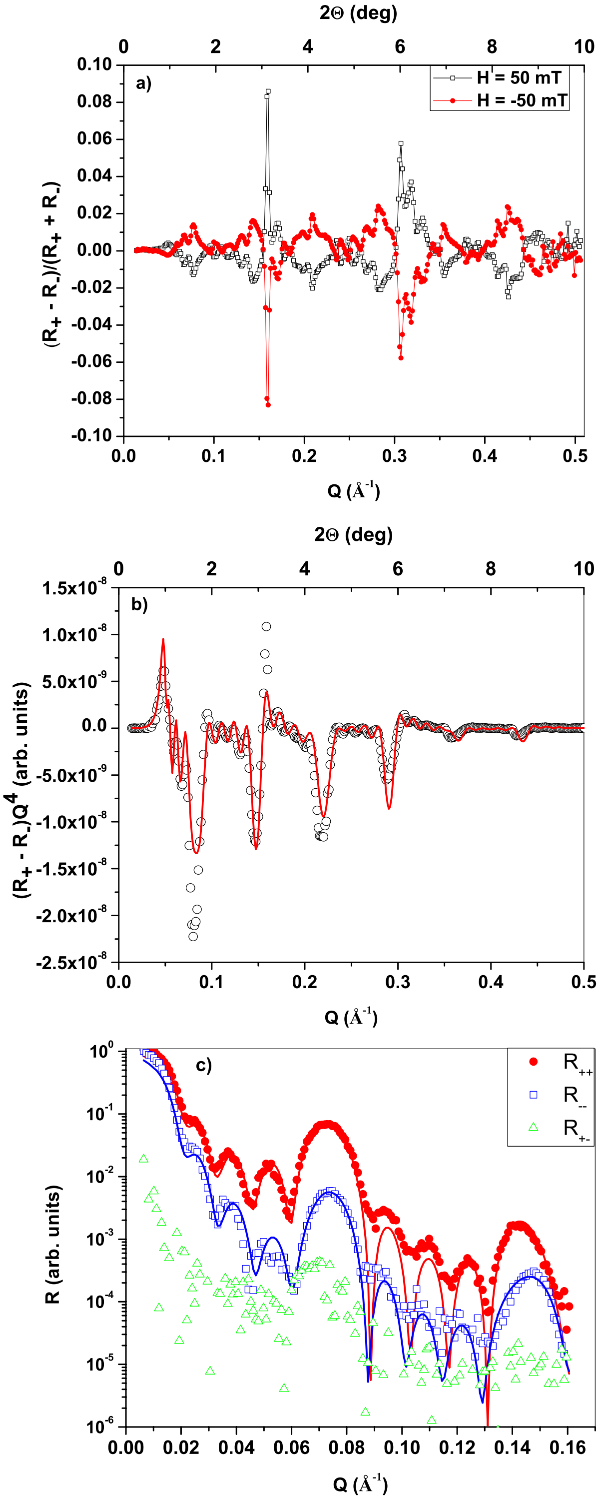

FIG. 6. (Color online) (a) Resonant x-ray magnetic reflectivity spectra (asymmetry ratio) measured at the Gd L_2 edge ($E=7929$ eV) at $T=140$ K in magnetic fields of 50 and −50 mT. The signals measured at opposite fields are symmetrical, which indicates their magnetic origin. (b) Experimental (circles) and fitted (line) RXMR spectra for $T=140$ K, $H=50$ mT. (c) Experimental (points) and fitted (lines) PNR spectra for $T=140$ K, $H=50$ mT. Since there is negligible signal in the spin-flip neutron channel, all the magnetic moments in the system are aligned along or opposite to the applied magnetic field.

C. Inhomogeneous magnetic states at low temperatures

Low-temperature ($T=20$ K) magnetic states were determined by simultaneous refinement of PNR and RXMR spectra. Preliminary PNR measurements performed at the POSY1 reflectometer at the Intense Pulsed Neutron Source (Argonne National Laboratory) with a position-sensitive detector have shown very strong spin-flip scattering (R_{+-}) at the first Bragg-peak position in the specular reflectivity channel, with a negligible off-specular signal. Upon repeating these measurements at the NG1 reflectometer (NIST), however, we detected rather weak specular but very strong off-specular scattering in the spin-flip channel, and little nonspecular signal in non-spin-flip channels. The off-specular spin-flip scattering indicates that the system was broken into a set of in-plane domains. However, the data in the non-spin-flip channels were reproducible, which indicates that the domains have the same projection of the magnetic moment along the direction of the magnetic field and varying projections perpendicular to the field. The size of these domains was not reproducible between measurements. Since the in-plane domain structure for the PNR measurement was not reproducible, and since our RXMR measurements were not sensitive to the perpendicular component of the magnetic moment, we did not analyze the spin-flip PNR data. Hence, the simultaneous refinement was carried out using RXMR and non-spin-flip PNR data.

The RXMR measurements performed on Fe/Gd multilayers of similar composition but with a larger (15) number of bilayers[16] revealed that at low temperatures the magnitude of the Gd magnetic moment does not change significantly within Gd layers, and the main effect is expected to be the change in the direction of the Gd moment. In our modeling of low-temperature magnetization profiles, we assume that the magnitude of the magnetic moment is constant within the Gd and Fe layers, and the behavior of the system can be described by the depth-dependent angle $\theta(z)$ between the direction of the magnetic moment and the applied magnetic field. The results of the refinements for two values of the applied magnetic field (50 and 500 mT) are shown in Figs. 8 and 9. The refined magnetization profiles are found highly inhomogeneous and are depicted in Fig. 7. In our data analysis, we found the PNR spectra to be very sensitive to the Gd intralayer structure. For example, the shift in the first Bragg-peak position for neutrons of different polarizations in Fig. 8(c) ($H=50$ mT) is directly related to the intralayer rotation of magnetic moments inside Gd. A similar effect observed by Hahn *et al.*[12] in Fe/Gd superlattices could not be modeled assuming uniformly magnetized Gd layers.

In order to double check our refinement results, we compare the element-specific net magnetic moments (integrated over the multilayer thickness) at $T=20$ K and 140 K for $H=50$ mT as obtained independently from SQUID/XMCD and PNR/RXMR measurements. Table III summarizes the magnetic-moment values obtained by using SQUID/XMCD data from Table II and integrating over the element-specific magnetization profiles of Fig. 7. We note reasonable agreement between the results obtained with the different methods.

V. DISCUSSION

The system under consideration [Fe(35 Å)/Gd(50 Å)]$_5$ has been previously investigated in detail for the case of a large (15) number of bilayers and different types of surface termination (both ends Fe, both ends Gd, and asymmetric termination Fe-Gd).[12,14–16] By comparing our results with the reported ones, we can identify common features that are typical of the system and unique features that were not observed in Fe/Gd multilayers with a large number of repetitions. First, the high-temperature properties well above the compensation temperature are found to be the same both in our system ($N=5$) and in Fe/Gd superlattices ($N=15$).[8,16] If the applied magnetic field is small enough (50 mT in our case),

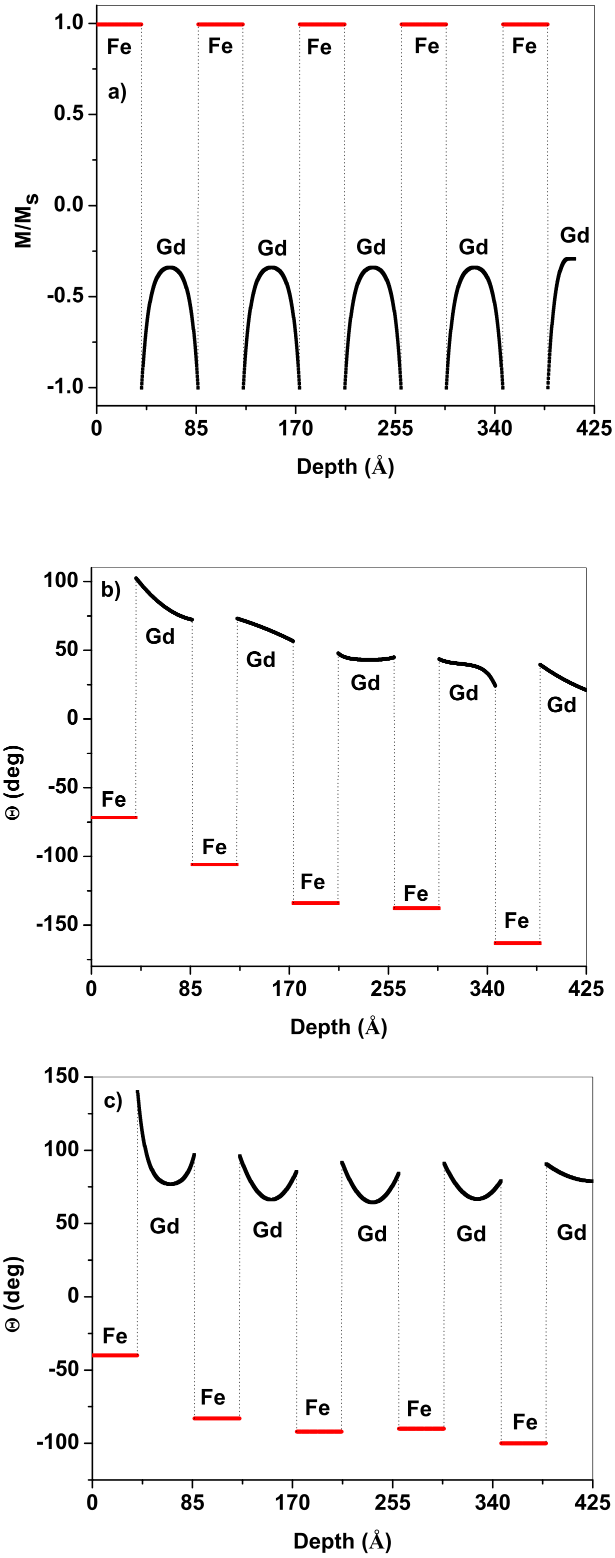

FIG. 7. (Color online) Refined magnetization profile within the Fe/Gd heterostructure (a) in the high-temperature Fe-aligned state ($T=140$ K, $H=50$ mT); in twisted low-temperature ($T=20$ K) states at (b) $H=50$ mT and (c) $H=500$ mT. The Fe-aligned state is described in terms of the depth-dependent value of magnetic moment. The twisted states are described in terms of the depth-dependent angle between the direction of magnetic moment and applied magnetic field.

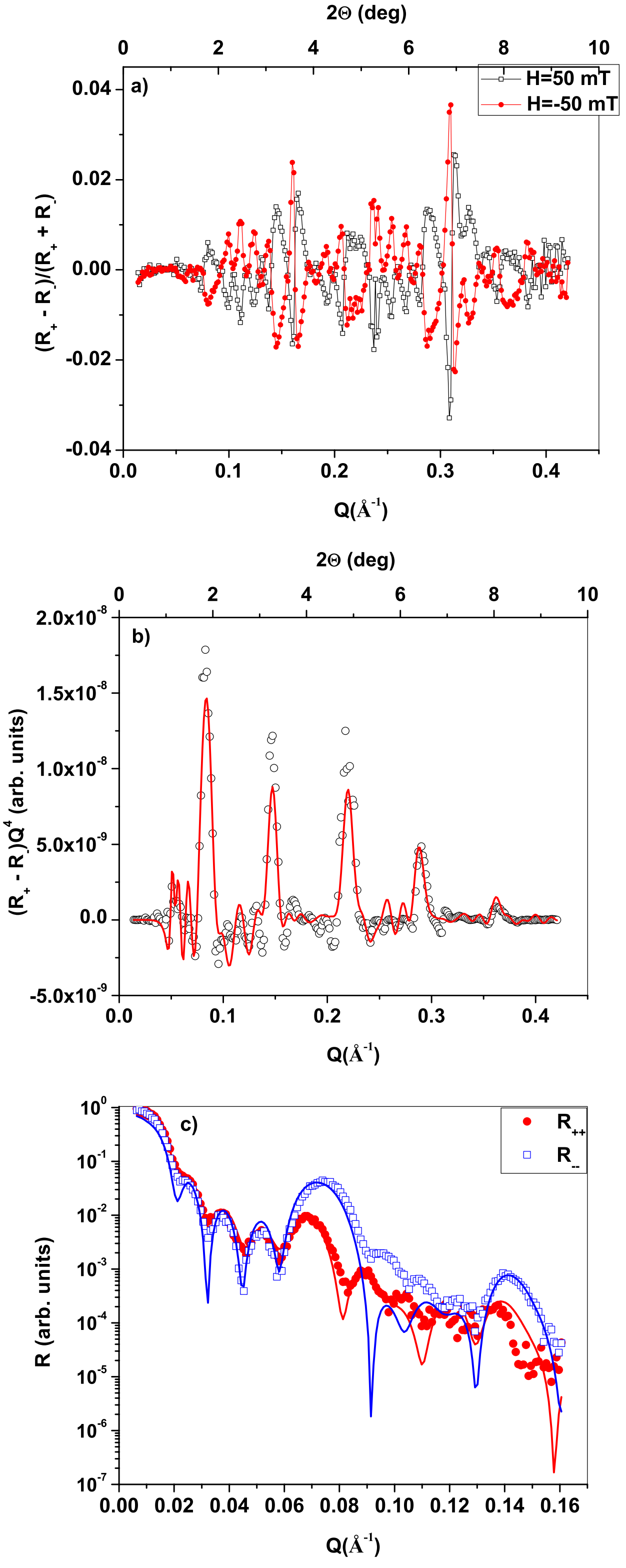

FIG. 8. (Color online) (a) Resonant x-ray magnetic reflectivity spectra (asymmetry ratio) measured at the Gd L_2 edge ($E=7929$ eV) at $T=20$ K in magnetic fields 50 and −50 mT. The signals measured at opposite fields are symmetrical, which indicates their magnetic origin. (b) Experimental (circles) and fitted (line) RXMR spectra for $T=20$ K, $H=50$ mT. (c) Experimental (points) and fitted (lines) non-spin-flip PNR spectra for $T=20$ K, $H=50$ mT.

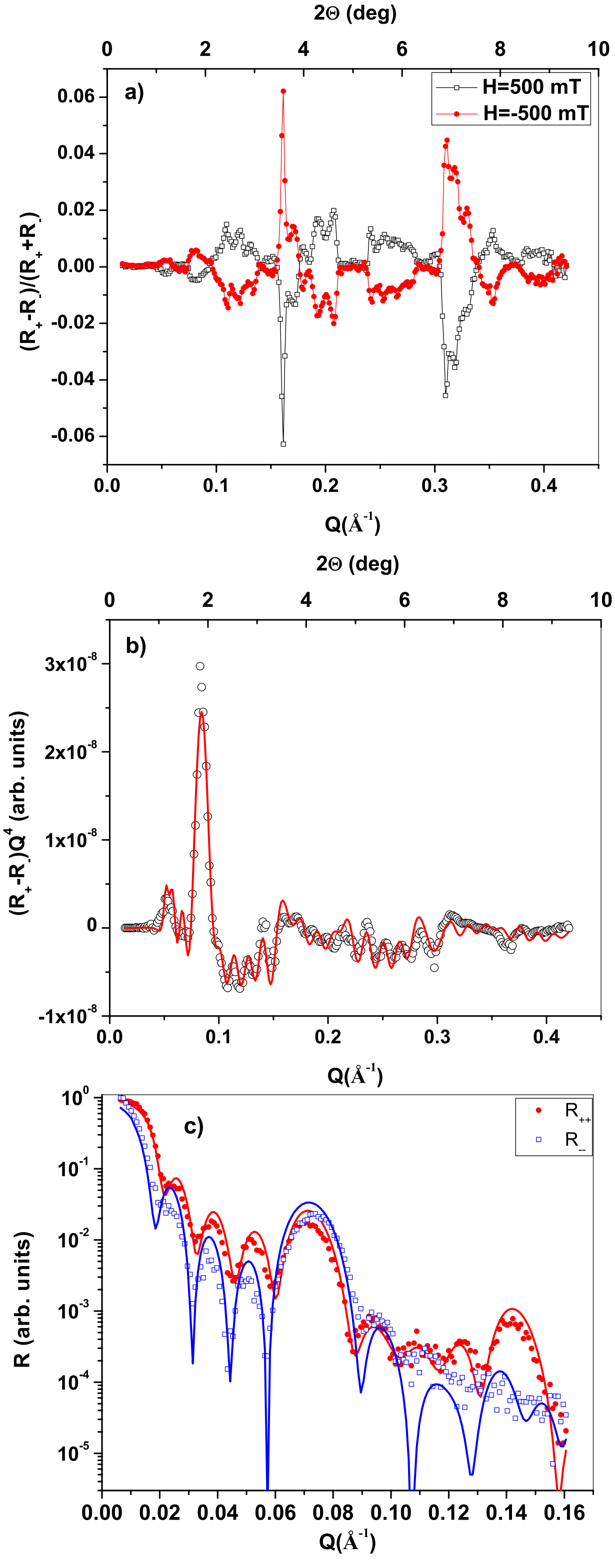

FIG. 9. (Color online) (a) Resonant x-ray magnetic reflectivity spectra (asymmetry ratio) measured at the Gd L_2 edge ($E=7929$ eV) at $T=20$ K in magnetic fields 500 and −500 mT. The signals measured at opposite fields are symmetrical, which indicates their magnetic origin. (b) Experimental (circles) and fitted (line) RXMR spectra for $T=20$ K, $H=500$ mT. (c) Experimental (points) and fitted (lines) non-spin-flip PNR spectra for $T=20$ K, $H=500$ mT.

TABLE III. Comparison of projections of Gd and Fe net magnetic moments along the magnetic field as reduced from SQUID/XMCD and PNR/RXMR data. The applied magnetic field value was 50 mT. The magnetic moments per unit area are given in absolute values (10^{-3} emu cm^{-2}).

T(K)	M_{Fe} (SQUID/XMCD)	M_{Fe} (PNR/RXMR)	M_{Gd} (SQUID/XMCD)	M_{Gd} (PNR/RXMR)
20	−1.68	−1.56	2.16	2.04
140	3.34	3.34	−2.75	−2.67

there exists the well-defined Fe-aligned phase with antiparallel alignment of Fe and Gd magnetic moments, with the Fe moment being along the magnetic field direction. The Gd magnetization profile is inhomogeneous due to the interfacial Fe-Gd proximity effect, with the perturbed interfacial region being about 4 Å in thickness, in agreement with Ref. 8. The magnetic moment in the core of the Gd layers scales with temperature, but the interfacial moment is close to its bulk value ($7.55\mu_B$) and temperature independent up to room temperature. This behavior seems to be typical of Fe/Gd heterostructures with any number of periods.

On the other hand, the low-temperature behavior was found to be different from that found in systems with $N=15$ bilayers. A Gd-aligned phase with antiparallel alignment of Fe and Gd magnetic moments was detected in $[\mathrm{Fe}(35\ \text{Å})/\mathrm{Gd}(50\ \text{Å})]_{15}$ superlattices at temperatures of 10–20 K and applied magnetic field of 50 mT,[15,16,41] i.e., well below the compensation temperature. When the number of bilayers becomes small, as in our system ($N=5$), the magnetic phase diagram is modified, and the Gd-aligned phase does not appear. According to our results at low field, the integrated Gd magnetic moment along the magnetic field is reduced ~20% compared to the saturated bulk value. Such reduction was sometimes reported for Fe/Gd multilayers[12,31] and was generally explained by a uniform reduction in the magnitude of Gd moment due to finite-size effects, or defects in the sample's microstructure. In our case, the magnetic behavior cannot be explained in terms of a Gd-aligned state with a reduced magnitude of Gd moment. At both low and high fields Gd and Fe magnetic moments are rotated away from the direction of magnetic field. As the applied magnetic field increases, the magnetization profile changes differently for Fe and Gd layers. As for Fe, the magnetic moments start rotating toward the direction of magnetic field; the strongest rotation is observed for the very top Fe layer which is exchange coupled to only one Gd layer, and the weakest rotation is seen for the very bottom Fe layer [Fig. 7(b)]. This type of rotation is known as a surface twist,[5–7] and it is typical of exchange-coupled multilayers with finite number of bilayers. As for Gd, its magnetic moment reacts to the applied field in a different way, namely, the intralayer magnetic-moment distribution changes. As the magnetic field increases, the magnetic moments in the core of Gd layers rotate toward the magnetic field, while the interface Gd moments try to maintain antiferromagnetic alignment with the neighboring Fe moments. Previous measurements were not able to directly probe the nature of these rotations with near-atomic resolution. In particular, Ref. 15 reported a rigid rotation of Gd magnetic moments at low temperatures without inhomogeneity in magnitude and/or direction of the moments within the Gd layers. On the other hand, Refs. 41 and 42 reported micromagnetic simulations of an inhomogeneous intralayer Gd magnetic structure in the twisted state in $[\mathrm{Fe}/\mathrm{Gd}]_{15}$ superlattices, but the absorption-based XMCD measurements could not directly resolve details of this twisted inhomogeneous structure.

VI. CONCLUSION

We have resolved element-specific complex magnetic structures in a $[\mathrm{Fe}(35\ \text{Å})/\mathrm{Gd}(50\ \text{Å})]_5$ multilayer as a function of temperature and magnetic field by performing simultaneous refinement of polarized neutron reflectometry and resonant x-ray magnetic reflectometry spectra. The complementary use of the PNR and RXMR techniques has made it possible to refine complex magnetization profiles in Fe/Gd heterostructures, including refinement of the inhomogeneous intralayer structure inside Gd. We stress the importance of such an approach, for it provides results that cannot be obtained by applying any of these techniques separately. A twisted phase is observed in this system ($N=5$) far below the compensation temperature even at low applied field, which differs significantly from observation in multilayer ($N=15$) where a Gd-aligned phase is observed.

ACKNOWLEDGMENTS

Work at Argonne is supported by the U.S. Department of Energy, Office of Science, Office of Basic Energy Sciences, under Contract No. DE-AC02-06CH11357. We thank Y. Choi, J. C. Lang, and J. Borchers for help with measurements.

APPENDIX A: RXMR CALCULATION SCHEME

The high magnetic spatial resolution of RXMR calls for performing data analysis with corresponding high precision in order to account for possible intralayer variations in the magnetic-moment density. Currently, experimental RXMR data are routinely analyzed within either the modified magnetic Parratt formalism[14] or the dynamical recursive matrix approach.[35] The last approach has later been generalized[36] to include structural and magnetic roughness within the distorted-wave Born approximation. Application of any of these approaches to RXMR data analysis implies splitting magnetic layers into thin slices, within which the magnetic moment is constant. The change in magnetic moment density from slice to slice is parametrized with a functional form with enough flexibility to accommodate the expected variations. The necessity of the slicing procedure makes data analysis of complex magnetic systems time consuming and dependent on the chosen slice thickness. When applied to complex magnetic systems with a large number of magnetically inhomogeneous layers, the slicing procedure often provides unstable solutions. In our approach we modified the dynamical formalism[35,36] in order to account for nonuniform intralayer distribution of magnetic moments without splitting the system into slices. The formalism is based on a characteristic matrix relating electrical and magnetic fields in neighboring layers. The contributions due to the parametrized nonuniform intralayer distribution of magnetic moments are directly included into the characteristic matrix.

The propagation of the x rays in a stratified media is described by the Maxwell equations,

$$[\vec{\nabla} \times \vec{E}] = i\frac{\omega}{c}\vec{H}, \tag{A1}$$

$$\vec{\nabla}(\vec{\nabla}\vec{E}) - \Delta\vec{E} + \frac{\omega^2}{c^2}(\varepsilon_c\vec{E} - i\varepsilon_m[\vec{m} \times \vec{E}]) = 0, \tag{A2}$$

where $\vec{m}$ is a unit vector in the direction of the magnetic moment, and ε_c and ε_m are charge and magnetic contributions to the dielectric permittivity, respectively. As is common in reflectometry, we relate the permittivity to charge and magnetic parts of the refractive index,

$$\varepsilon_c = 1 - 2\delta_c + i2\beta_c, \quad \varepsilon_m = 2\delta_m - i2\beta_m. \tag{A3}$$

In our theoretical consideration, we limit ourselves to first-order terms in the magnetic part of the refractive index.

Let (xz) be the scattering plane. Then the electric field vector $\vec{E}$ in the multilayer will have the form,

$$\vec{E}(x,z) = \vec{\mathbf{E}} \exp\left(-i\frac{\omega}{c}[x\cos\theta + zn(z)]\right), \tag{A4}$$

where θ is the incidence angle and $\frac{\omega}{c}n(z)$ is the depth-dependent normal component of the wave vector. Split the system in a set of uniform layers; within each of them the parameter n is constant. In order for the system [Eqs. (A1) and (A2)] to have a solution, n within a layer should satisfy the equation,

$$\begin{aligned}\varepsilon_c(\varepsilon_c - \cos^2\theta - n^2)^2 - \varepsilon_m^2(\varepsilon_c - \cos^2\theta - n^2)\\ - \varepsilon_m^2(m_x\cos\theta + m_z n)^2 = 0.\end{aligned} \tag{A5}$$

To the first order in ε_m, n in a layer can be found as

$$n_\pm^2 = n_c^2 \pm \frac{\varepsilon_m}{\sqrt{\varepsilon_c}}(m_x\cos\theta + m_z n_c), \tag{A6}$$

where $n_c = \sqrt{\varepsilon_c - \cos^2\theta}$. Away from the charge-critical edge, the parameter n can be decomposed into the sum of charge and magnetic parts,

$$n_\pm = n_c \pm n_m, \qquad n_m = \frac{\varepsilon_m}{2n_c\sqrt{\varepsilon_c}}(m_x\cos\theta + m_z n_c). \tag{A7}$$

By using boundary conditions for E_x, E_y, H_x, and H_y,[35,36] and eliminating consecutively the E coefficients inside the layers, we come to the following matrix equation relating incidence (I), reflection (R), and transmission (T) coefficients:

$$\begin{pmatrix} I_\sigma + R_\sigma \\ \sin\theta[I_\sigma - R_\sigma] \\ I_\pi + R_\pi \\ \sin\theta[I_\pi - R_\pi] \end{pmatrix} = \hat{M}_1\hat{M}_2 \ldots \hat{M}_N \begin{pmatrix} T_\sigma \\ n_s T_\sigma \\ \sqrt{\varepsilon_s}T_\pi \\ n_s/\sqrt{\varepsilon_s}T_\pi \end{pmatrix}. \tag{A8}$$

The 4×4 characteristic matrices $\hat{M}_i$, describing the properties of individual layers, have the following form:

$$\hat{M} = \begin{pmatrix} \widehat{A_{\sigma\sigma}} & -i\widehat{A_{\sigma\pi}} \\ i\widehat{A_{\pi\sigma}} & \widehat{A_{\pi\pi}} \end{pmatrix}, \tag{A9}$$

where

$$\widehat{A_{\sigma\sigma}} = \begin{pmatrix} \cos(k_0n_ct) & i/n_c\sin(k_0n_ct) \\ in_c\sin(k_0n_ct) & \cos(k_0n_ct) \end{pmatrix},$$

$$\widehat{A_{\pi\pi}} = \begin{pmatrix} \cos(k_0n_ct) & i\varepsilon_c/n_c\sin(k_0n_ct) \\ in_c/\varepsilon_c\sin(k_0n_ct) & \cos(k_0n_ct) \end{pmatrix},$$

$$\begin{aligned}\widehat{A_{\sigma\pi}} = \sin(k_0n_m)&\begin{pmatrix} \sin(k_0n_ct)/\sqrt{\varepsilon_c} & -i\sqrt{\varepsilon_c}/n_c\cos(k_0n_ct) \\ -in_c/\sqrt{\varepsilon_c}\cos(k_0n_ct) & \sin(k_0n_ct)\sqrt{\varepsilon_c} \end{pmatrix}\\ &+ \frac{n_m}{n_c}\begin{pmatrix} 0 & i\sqrt{\varepsilon_c}/n_c\sin(k_0n_ct) \\ -in_c/\sqrt{\varepsilon_c}\sin(k_0n_ct) & 0 \end{pmatrix},\end{aligned}$$

$$\begin{aligned}\widehat{A_{\pi\sigma}} = \sin(k_0n_m)&\begin{pmatrix} \sin(k_0n_ct)\sqrt{\varepsilon_c} & -i\sqrt{\varepsilon_c}/n_c\cos(k_0n_ct) \\ in_c/\sqrt{\varepsilon_c}\cos(k_0n_ct) & \sin(k_0n_ct)/\sqrt{\varepsilon_c} \end{pmatrix}\\ &+ \frac{n_m}{n_c}\begin{pmatrix} 0 & i\sqrt{\varepsilon_c}/n_c\sin(k_0n_ct) \\ -in_c/\sqrt{\varepsilon_c}\sin(k_0n_ct) & 0 \end{pmatrix},\end{aligned}$$

where t is the layer thickness.

Consider a magnetically inhomogeneous resonant layer where the charge permittivity ϵ_c is constant but the magnetic part $\epsilon_m(z)$ is position dependent. This dependence may be due to any kind of magnetic inhomogeneity, including both changes in the magnitude or direction of the magnetic moment. If the layer is split into a set of infinitely thin sublayers, and the product of transition matrices of these sublayers is calculated, keeping only the first-order terms in ϵ_m, then the net characteristic matrix for this magnetically inhomogeneous layer will again have the form of Eq. (A9), but now the off-diagonal magnetic matrices $\widehat{A_{\sigma\pi}}$ and $\widehat{A_{\pi\sigma}}$ have to be modified,

$$\begin{aligned}\widehat{A_{\sigma\pi}} = I_0&\begin{pmatrix} \sin(k_0n_ct)/\sqrt{\varepsilon_c} & -i\sqrt{\varepsilon_c}/n_c\cos(k_0n_ct) \\ -in_c/\sqrt{\varepsilon_c}\cos(k_0n_ct) & \sin(k_0n_ct)\sqrt{\varepsilon_c} \end{pmatrix}\\ &+ \begin{pmatrix} I_1/\sqrt{\varepsilon_c} & -i\sqrt{\varepsilon_c}/n_cI_2 \\ -in_c/\sqrt{\varepsilon_c}I_2 & -\sqrt{\varepsilon_c}I_1 \end{pmatrix},\end{aligned} \tag{A10}$$

$$\widehat{A_{\pi\sigma}} = I_0\begin{pmatrix} \sin(k_0 n_c t)\sqrt{\varepsilon_c} & -i\sqrt{\varepsilon_c}/n_c \cos(k_0 n_c t) \\ i n_c/\sqrt{\varepsilon_c} \cos(k_0 n_c t) & \sin(k_0 n_c t)/\sqrt{\varepsilon_c} \end{pmatrix} + \begin{pmatrix} I_1/\sqrt{\varepsilon_c} & -i\sqrt{\varepsilon_c}/n_c I_2 \\ -i n_c/\sqrt{\varepsilon_c} I_2 & -\sqrt{\varepsilon_c} I_1 \end{pmatrix}. \tag{A11}$$

In this equation we introduced the following parameters:

$$I_0 = k_0 \int_0^t n_m(z) dz, \tag{A12}$$

$$I_1 = k_0 \int_0^t n_m(z) \sin(k_0 n_c [t - 2z]) dz, \tag{A13}$$

$$I_2 = k_0 \int_0^t n_m(z) \cos(k_0 n_c [t - 2z]) dz. \tag{A14}$$

Equations (A12)–(A14) are very convenient for calculations because they allow easy parametrization of the distribution of magnetic moments with a probe analytical function without a need for slicing.

As seen from the formulas above, the resonant magnetic signal depends both on the total integrated magnetic moment as well as on the variations in magnetic moments inside the resonant layers, with symmetric and antisymmetric parts of the magnetization profile contributing in different ways. The RXMR is sensitive to intralayer variations in the magnetic moments, even if the total integrated magnetic moment is zero. In performing experimental data analysis, it is useful to split the magnetic moment density profile into symmetric and antisymmetric parts.

In the case of small-incidence angles, typical for hard x rays, the difference between σ and π polarizations becomes negligible, and the calculation of the total characteristic matrix $\hat{M}_i$ can be performed by using 2×2 matrices only,

$$\hat{M} = \begin{pmatrix} \hat{A} & -i\hat{B} \\ i\hat{B} & \hat{A} \end{pmatrix}, \tag{A15}$$

where

$$\hat{A} = \prod_{i=1}^{N} \widehat{A_{\sigma\sigma}^{(i)}}; \quad \hat{B} = \sum_{i=1}^{N} \left(\prod_{j=1}^{i-1} \widehat{A_{\sigma\sigma}^{j}} \right) \widehat{A_{\sigma\pi}^{i}} \left(\prod_{k=i+1}^{N-i} \widehat{A_{\sigma\sigma}^{k}} \right). \tag{A16}$$

By mutilating characteristic matrices for all the layers in the system, the total characteristic matrix can be found and Eq. (A8) resolved relative to the reflection coefficients (R_+ and R_-) for two different helicities of the incoming x-ray beam. The difference between these two coefficients $\Delta R = R_+ - R_-$ was used in Eq. (4) in order to fit experimental RXMR data.

---

[1] *Nanomagnetism: Ultrathin Films, Multilayers and Nanostructures*, edited by D. L. Mills and J. A. C. Bland (Elsevier, New York, 2006).

[2] J. P. Andrés, L. Chico, J. Colino, and J. M. Riveiro, Phys. Rev. B **66**, 094424 (2002).

[3] V. L. B. de Jesús, I. S. Oliveira, P. C. Riedi, and A. P. Guimares, J. Magn. Magn. Mater. **212**, 125 (2000).

[4] J. Landes, Ch. Sauer, B. Kabius, and W. Zinn, Phys. Rev. B **44**, 8342 (1991).

[5] R. E. Camley and D. R. Tilley, Phys. Rev. B **37**, 3413 (1988).

[6] R. E. Camley, Phys. Rev. B **39**, 12316 (1989).

[7] J. G. LePage and R. E. Camley, Phys. Rev. Lett. **65**, 1152 (1990).

[8] D. Haskel, G. Srajer, J. C. Lang, J. Pollmann, C. S. Nelson, J. S. Jiang, and S. D. Bader, Phys. Rev. Lett. **87**, 207201 (2001).

[9] K. Engl, W. Brunner, and J. Zweck, J. Phys.: Condens. Matter **14**, 10033 (2002).

[10] *Modern Techniques for Characterizing Magnetic Materials*, edited by Y. Zhu (Kluwer Academic Publishers, Boston, 2005).

[11] C. Dufour, K. Cherifi, G. Marchal, Ph. Mangin, and M. Hennion, Phys. Rev. B **47**, 14572 (1993).

[12] W. Hahn, M. Loewenhaupt, Y. Y. Huang, G. P. Felcher, and S. S. P. Parkin, Phys. Rev. B **52**, 16041 (1995).

[13] O. F. K. McGrath, N. Ryzhanova, C. Lacroix, D. Givord, C. Fermon, C. Miramond, G. Saux, S. Young, and A. Vedyayev, Phys. Rev. B **54**, 6088 (1996).

[14] N. Ishimatsu, H. Hashizume, S. Hamada, N. Hosoito, C. S. Nelson, C. T. Venkataraman, G. Srajer, and J. C. Lang, Phys. Rev. B **60**, 9596 (1999).

[15] N. Hosoito, H. Hashizume, N. Ishimatsu, I.-T. Bae, G. Srajer, J. C. Lang, C. K. Venkataraman, and C. S. Nelson, Jpn. J. Appl. Phys. Part 1 **41**, 1331 (2002).

[16] Y. Choi, D. Haskel, R. E. Camley, D. R. Lee, J. C. Lang, G. Srajer, J. S. Jiang, and S. D. Bader, Phys. Rev. B **70**, 134420 (2004).

[17] S. Demirtas, M. R. Hossu, R. E. Camley, H. C. Mireles, and A. R. Koymen, Phys. Rev. B **72**, 184433 (2005).

[18] R. E. Camley, W. Lohstroh, G. P. Felcher, N. Hosoito, and H. Hashizume, J. Magn. Magn. Mater. **286**, 65 (2005).

[19] J. P. Andrés, J. A. González, T. P. A. Hase, B. K. Tanner, and J. M. Riveiro, Phys. Rev. B **77**, 144407 (2008).

[20] A. Barth, F. Treubel, M. Marszałek, W. Evenson, O. Hellwig, C. Borschel, M. Albrecht, and G. Schatz, J. Phys.: Condens. Matter **20**, 395232 (2008).

[21] B. B. Van Aken, J. L. Prieto, and N. D. Mathur, J. Appl. Phys. **97**, 063904 (2005).

[22] S. Roy *et al.*, Phys. Rev. Lett. **95**, 047201 (2005).

[23] S. J. May, A. B. Shah, S. G. E. te Velthuis, M. R. Fitzsimmons, J. M. Zuo, X. Zhai, J. N. Eckstein, S. D. Bader, and A. Bhattacharya, Phys. Rev. B **77**, 174409 (2008).

[24] J. E. Lynn and P. A. Seeger, At. Data Nucl. Data Tables **44**, 191 (1990).

[25] S. W. Lovesey and S. P. Collins, *X-ray Scattering and Absorption in Magnetic Materials* (Oxford University Press, New York, 1996).

[26] The x-ray scattering parameters were taken from the web site of the NIST Center for X-ray Optics: http://henke.lbl.gov/optical_constants/.

[27] L. T. Baczewski, P. Pankowski, A. Wawro, K. Mergia, S. Messoloras, and F. Ott, Phys. Rev. B **74**, 075417 (2006).

[28] K. Hirano, T. Ishikawa, and K. Kikuta, Rev. Sci. Instrum. **66**, 1604 (1995).

[29] J. C. Lang and G. Srajer, Rev. Sci. Instrum. **66**, 1540 (1995).

[30] Here and below we use emu cm^{-2} and emu cm^{-3} units to measure magnetic moment per unit surface and per unit volume, respectively. To convert in SI units, $1\ \mathrm{emu\ cm}^{-3} = \mathrm{kA\ m}^{-1}$ and $1\ \mathrm{emu\ cm}^{-2} = 10\ \mathrm{A}$.

[31] C. Dufour, Ph. Bauer, M. Sajieddine, G. Marchal, and Ph. Mangnin, J. Magn. Magn. Mater. **121**, 300 (1993).

[32] *Neutron Scattering from Magnetic Materials*, edited by T. Chatterji (Elsevier, New York, 2006).

[33] S. J. Blundell and J. A. C. Bland, Phys. Rev. B **46**, 3391 (1992).

[34] A. Rühm, B. P. Toperverg, and H. Dosch, Phys. Rev. B **60**, 16073 (1999).

[35] S. A. Stepanov and S. K. Sinha, Phys. Rev. B **61**, 15302 (2000).

[36] D. R. Lee, S. K. Sinha, D. Haskel, Y. Choi, J. C. Lang, S. A. Stepanov, and G. Srajer, Phys. Rev. B **68**, 224409 (2003).

[37] Ph. R. Bevington and D. K. Robinson, *Data Reduction and Error Analysis for the Physical Sciences*, 2nd ed. (McGraw-Hill, Inc., New York, 1992).

[38] The minimization package MINUIT is freely available from CERN program library (CERNlib) under the GNU Public License (GPL): http://wwwinfo.cern.ch/asdoc/minuit/minmain.html.

[39] D. T. Cromer and D. Liberman, J. Chem. Phys. **53**, 1891 (1970).

[40] J. O. Cross, M. Newville, J. J. Rehr, L. B. Sorensen, C. E. Bouldin, G. Watson, T. Goulder, G. H. Lander, and M. I. Bell, Phys. Rev. B **58**, 11215 (1998).

[41] D. Haskel, G. Srajer, Y. Choi, D. R. Lee, J. C. Lang, J. Meersschaut, J. S. Jiang, and S. D. Bader, Phys. Rev. B **67**, 180406(R) (2003).

[42] Y. Choi, D. Haskel, A. Cady, J. C. Lang, D. R. Lee, G. Srajer, J. S. Jiang, and S. D. Bader, Phys. Rev. B **73**, 174401 (2006).